Hwang et al. *NPG Asia Materials* (2022) 14:72
https://doi.org/10.1038/s41427-022-00420-5

NPG Asia Materials

ARTICLE Open Access

Reactive oxygen species-generating hydrogel platform for enhanced antibacterial therapy

Changha Hwang[1], Min-Ha Choi[2], Hyoun-Ee Kim[1,3], Seol-Ha Jeong[1] and Ji-Ung Park[2]

Abstract

Zinc oxide nanoparticles (ZnO) have attracted much attention as promising antibacterial agents due to their ability to generate reactive oxygen species (ROS) that effectively eliminate bacteria. However, when they are delivered inside the body, this distinct characteristic of ROS is restricted due to the limited penetration depth of external light, which is required for the photocatalysis of particles. To produce ROS without any light source when the particles are implanted, we introduced catechol-ZnO complexes to a hyaluronic acid (HA) hydrogel platform, which can self-generate sufficient ROS in the bacteria-infected tissue. Catechol-ZnO complexes enhanced ROS generation via electron transfer from the formation of complexes and *o*-semiquinone, and a hydrogel structure was created by coordinate bonds between functionalized catechol groups in HA and ZnO simultaneously. This hydrogel demonstrated different behaviors in terms of physical properties compared to chemically cross-linked HA hydrogels containing ZnO. This hydrogel showed a higher swelling ratio, enzymatic degradation resistance, and tissue adhesive strength. Enhanced ROS generation was confirmed using electron paramagnetic resonance (EPR), H_2O_2 concentration, glutathione depletion, and intracellular ROS detection. The improved antibacterial performance of hydrogels from ROS production was also confirmed through in vitro bacterial testing against two bacterial strains, *E. coli* and *S. aureus*. Furthermore, an in vivo experiment using an infected mouse model to analyze colony formation, histologic analysis, and hematological inflammatory markers revealed the effective antibacterial effects of catechol-ZnO complexes. Overall, the potential of the hydrogel created via catechol-ZnO complexes for antibacterial therapy was demonstrated through the capability to enhance ROS generation and eradicate bacteria.

Introduction

Over the last few decades, the general approach to antibacterial therapeutics has been to utilize photocatalysts including metal oxide nanoparticles such as titanium oxide (TiO_2), copper oxide (CuO), and ZnO[1]. In particular, ZnO nanoparticles have shown great promise in biomedical applications due to their distinct characteristics[2]. ZnO nanoparticles have superior photocatalytic properties under light irradiation derived from their semiconductor structure and surface defects, which results in the production of reactive oxygen species (ROS)[3–5]. ROS, including hydroxyl radicals (•OH), singlet oxygen ($^1O_2$), superoxide anions ($O_2^{\bullet-}$), and hydrogen peroxide (H_2O_2), play essential roles in antibacterial functions through oxidative damage to DNA and the membrane of bacteria[6]. Moreover, Zn ions (Zn^{2+}) released from ZnO nanoparticles also play an important role in regulating cellular functions and interfere with bacterial growth[7,8]. However, the photocatalytic activity from ZnO nanoparticles is restricted to the external light intensity and range of the wavelength[9]. Furthermore, when ZnO nanoparticles are delivered inside the skin tissue for antibacterial therapeutics, the photocatalytic activity under light irradiation is limited due to the insufficient penetration depth of UV and visible light into the skin[10,11].

Catechol, which is sourced from the protein of marine mussels[12], has high adhesion properties with metal oxide

Correspondence: Seol-Ha Jeong (jsh528@snu.ac.kr) or Ji-Ung Park (alfbskan@gmail.com)
[1]Department of Materials Science and Engineering, Seoul National University, Seoul 08826, Republic of Korea
[2]Department of Plastic and Reconstructive Surgery, Seoul National University Boramae Medical Center, Seoul National University College of Medicine, Seoul 07061, Republic of Korea
Full list of author information is available at the end of the article

surfaces and has strong ROS generation properties, making it a strong candidate for biomedical application[13,14]. In recent studies, metal oxide nanoparticles have been introduced to form metal-mediated catechol complexes that obtain synergetic properties from both metal oxide and catechol characteristics[15]. The anchoring ability of catechol on the surface of metal oxide nanoparticles leads to the creation of reversible coordinate bonds[16]. Furthermore, previous studies have shown that metal-mediated catechol complexes produce ROS through the oxidation process[17]. The electron transfer during the oxidation from catechol to *o*-semiquinone, in which the metal oxide nanoparticles act as catalysts, transforms oxygen molecules into ROS[18,19]. ROS generation and metal ion release from metal oxide nanoparticles could affect the cellular response and antibacterial activity[20]. Zhongtian Zhang et al. presented ROS generation via electron transfer during o-semiquinone formation, which transforms O_2 into $O_2^{\bullet-}$ and the oxidation process from $O_2^{\bullet-}$ to $^1O_2$ by iron oxide nanoparticles, and verified the antibacterial effect by generating ROS from the structure. However, the use of these microgels for real antibacterial applications is limited due to the high toxicity of iron nanoparticles. Therefore, we hypothesize that catechol-metal oxide nanoparticle complexes, which possess good biocompatibility and biodegradability, could improve the efficacy of killing bacteria while increasing ROS generation compared to metal oxide nanoparticles themselves under visible light irradiation and could be used for real biomedical applications.

To use catechol-metal oxide nanoparticle complexes as ROS carriers in the form of an implantable therapeutic nanoplatform, we utilized an injectable hydrogel network because its high water content and porosity enable the delivery of ROS to the targeted tissue. In this work, we introduce a ROS-releasing nanoengineered hydrogel made of a combination of HA hydrogel and ZnO nanoparticles. HA, a polysaccharide that naturally exists in the human body, is used as a backbone of hydrogels because of its nonimmunogenic, biocompatible, and degradable nature[21]. In addition, the catechol group is introduced, which takes advantage of the HA's various functional groups that enable cross-linking of the hydrogel network via catechol-ZnO nanoparticle complexes[22]. It is expected that ZnO nanoparticles can simultaneously act as both antibacterial therapeutic agents and cross-linker agents. In this study, the hydrogel characteristics derived from coordinate bonds between catechol and ZnO nanoparticles were examined. The mechanical properties of the hydrogels were verified by monitoring the rheological behaviors, swelling ratio, degradation profiles, and adhesive strength. Furthermore, the ROS generation ability was determined using electron paramagnetic resonance (EPR), H_2O_2 concentration, glutathione (GSH) depletion, and intracellular ROS detection (DCFDA) assays. The enhanced antibacterial performance of the hydrogel was also demonstrated with both *Escherichia coli* (*E. coli*) and *Staphylococcus aureus* (*S. aureus*) strains using in vitro experiments. Finally, in vivo analysis of the antibacterial effect of the hydrogel, including colony formation, histologic analysis, and hematological inflammatory marker analysis, was performed using a subcutaneous abscess model in mice.

Results and discussion

Synthesis and characterization of HCZ hydrogels

Figure 1a, b illustrates the fabrication process of catechol-modified hyaluronic acid (HA-CA)-ZnO complex (HCZ)-based hydrogels (HCZ hydrogels). First, HA-CA was prepared with EDC/NHS coupling agents (Fig. 1a). Functionalized catechol from HA-CA was identified by ^{1}H-NMR spectroscopy (Fig. S1).

The peaks between $\delta = 6.7$ ppm and $\delta = 7.0$ ppm correspond to the characteristic peaks of dopamine, and they indicate the protons in the ortho- and meta-coupling positions of the aromatic ring, respectively[23]. The conjugation ratio of HA-CA was calculated using UV−Vis spectroscopy, as depicted in Fig. S1c. To calculate the conjugation ratio of dopamine on HA, dopamine standard curves were obtained at 280 nm. Based on the measured absorbance of HA-CA at ~280 nm, the concentration of dopamine was 0.256 mM. Consequently, the degree of conjugated dopamine was 9.9%. Next, ZnO nanoparticles were fabricated using a precipitation method at room temperature. As shown in the TEM images in Fig. S2, the average diameter of ZnO nanoparticles was 34.1 ± 10.4 nm. Consequently, the mixture of HA-CA and ZnO nanoparticles was cured at 50 °C for 24 h to fabricate hydrogels based on catechol-ZnO complexes (Fig. 1b). The phase transition from sol to gel of HCZ hydrogels proceeded as shown in Fig. 1c. After gelation, the color of the HCZ hydrogel changed from gray to black. Temperatures elevated above room temperature were expected to accelerate the reaction rate of cross-linking on the surface of ZnO nanoparticles with catechol. The porous morphology determined from SEM images revealed the formation of a hydrogel structure (Fig. S3). As shown by the high magnification SEM images in Fig. S4, we could detect the ZnO nanoparticles on the surface of the hydrogels. In this hydrogel structure, a ZnO nanoparticle acted as a cross-linker via the coordinate bond between the catechol moiety and the particle. Multivalent coordinate bonds of catechol with metal oxide nanoparticles can create a cross-linking system that produces the hydrogel matrix[16]. To identify the characteristics derived from catechol-ZnO complexes, chemically cross-linked HA hydrogels containing 3 wt% ZnO nanoparticles (HAZ hydrogels) were established as another experimental group (Fig. 1d).

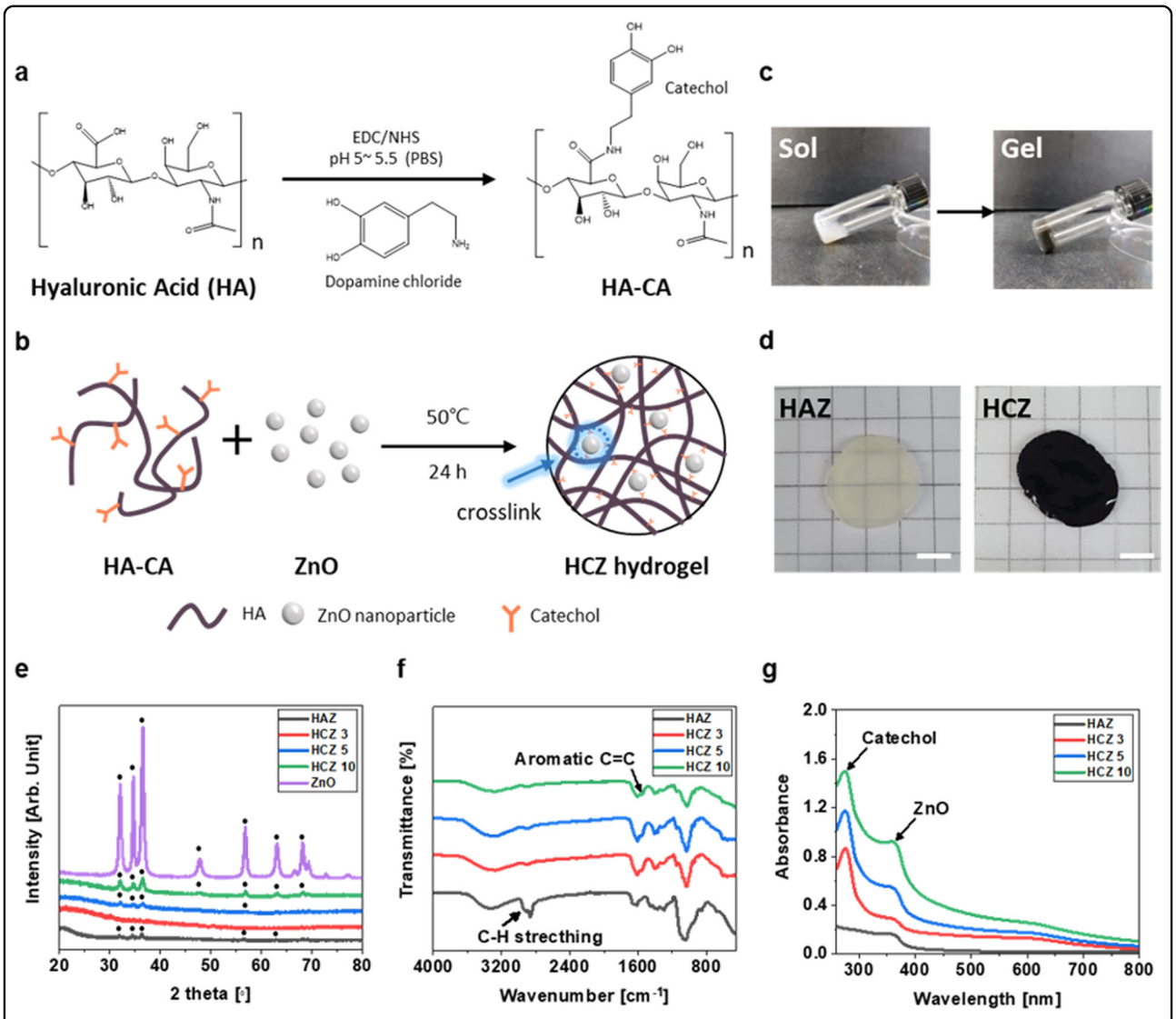

Fig. 1 Process of HA-CA synthesis and characterization of HCZ hydrogels. Schematic illustrations of **a** synthesis of HA-CA polymer and **b** preparation of HCZ hydrogel. **c** Phase transition images of HCZ hydrogel. **d** Photographs of HAZ (left) and HCZ hydrogel (right). (Scale bar: 1 cm) **e** XRD patterns, f FT-IR spectra, and **g** UV–vis absorption spectra of HAZ and HCZ hydrogels.

The XRD diffraction patterns in Fig. 1e show the crystallinity of ZnO nanoparticles and hydrogels with different concentrations of ZnO nanoparticles. The high crystallinity of the synthesized ZnO nanoparticles was proven simply by observing the characteristic peaks of ZnO. In the case of HCZ hydrogels, the ZnO-related peak intensity increased with the ZnO nanoparticle content. Figure 1f shows the FT-IR spectra of hydrogels that were used to examine the chemical structure according to the crosslinking system. The C-H stretching peak at 2856 cm^{-1} was observed in the HAZ hydrogel, and this peak was attributed to the chemical crosslinker BDDE. The catechol moieties of HCZ hydrogels were determined by the aromatic C=C peaks at 1563 cm^{-1}. The UV–vis absorption spectra of the hydrogels are presented in Fig. 1g. The absorbance bands of conjugated catechol and ZnO nanoparticles were observed at approximately 280 nm and 360 nm, respectively, in the hydrogels. The absorbance peak of the ZnO nanoparticles was assigned to the intrinsic band gap energy absorption[24]. In addition, the increased absorbance of HCZ hydrogels was inspected in a range of visible light due to the interfacial charge transfer from the formation of coordination geometry between catechol and ZnO. At the interface of HA-CA and ZnO nanoparticles, unique interfacial charge transitions can occur via the chelating linkage between the catechol moiety and ZnO surface[25]. As the concentration of ZnO nanoparticles increased, a stronger absorption

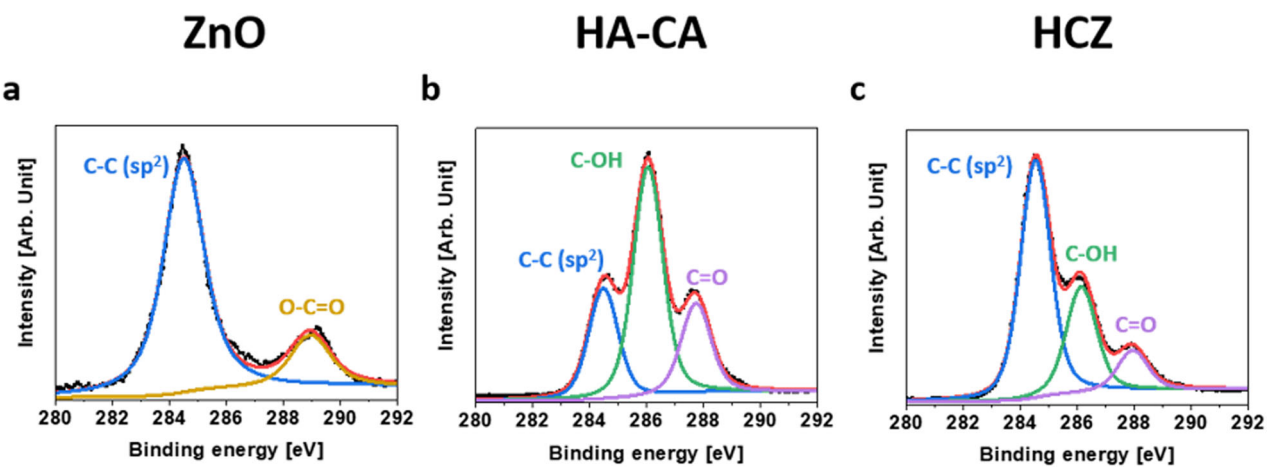

Fig. 2 XPS data of the samples. High resolution XPS spectra of the carbon region (C 1s) for **a** the ZnO nanoparticles, **b** HA-CA, and **c** HCZ hydrogel, respectively.

band was observed in the visible light spectrum due to the acquisition of more bidentate or monodentate bridge structures. The zeta potential and hydrodynamic diameter of HCZ were also examined, as shown in Fig. S5. These values were correlated with the homogeneity and dispersity of the polymer-nanoparticle mixture[26]. The zeta potential of HCZ (−36.9 ± 0.5 mV) was higher than that of ZnO (−23.3 ± 1.4 mV), which indicated that HCZ had a more negatively charged surface due to the presence of HA and created one phase via the coordinate bond between catechol and ZnO nanoparticles. The hydrodynamic diameter of HCZ was also drastically increased compared with that of ZnO nanoparticles alone due to the formation of cross-linking between HA-CA and ZnO nanoparticles.

To elucidate the chemical structure of HCZ hydrogels, high-resolution XPS C 1s spectra of ZnO, HA-CA, and HCZ were measured, and they are shown in Fig. 2. From Fig. 2a, the carbon peaks that were detected in ZnO nanoparticles, such as C–C (sp^2) at 284.4 eV and O–C=O at 288.9 eV, were related to adventitious carbon contamination due to exposure to an ambient environment. C–OH (285.9 eV) and C=O peaks (287.8 eV) were observed in HA-CA, and these peaks were attributed to the functionalization of catechol groups (Fig. 2b). After HA-CA mixed with ZnO nanoparticles, which created catechol-ZnO complexes in the HCZ hydrogel, the intensity of C–OH and C=O peaks decreased, as shown in Fig. 2c. This indicates that the coordinate bonds between catechol and ZnO nanoparticles were successfully created, which contributed to the gelation of the HCZ hydrogel.

The ZnO nanoparticle content affected the rheological behavior of the HCZ hydrogel, as illustrated in Fig. 3a and Fig. S6. The storage modulus was obtained using a frequency sweep mode to illustrate the mechanical stiffness. The storage modulus at a certain frequency (1 rad/s) was substantially increased from 108.1 ± 44.5 to 290 ± 16.0 Pa as the incorporation of ZnO nanoparticles in HCZ hydrogels increased from 3 to 10 wt%. This revealed that the incorporation of more ZnO nanoparticles increased the cross-link density due to the participation of ZnO nanoparticles as a crosslinker. The HAZ hydrogel showed 173.4 ± 30.4 Pa at 1 rad/s frequency, which was similar to the values shown by HCZ hydrogels.

The swelling behaviors of HCZ and HAZ hydrogels were dependent on the concentration and type of crosslinker, as shown in Fig. 3b. The swelling ratio of HCZ hydrogels decreased from 106.7 ± 4.7 to 91.7 ± 2.2 after 72 h of incubation with increasing amounts of ZnO nanoparticles. A high concentration of ZnO nanoparticles increases the cross-linking density by providing more cross-linking sites. Surprisingly, HAZ hydrogels showed a lower swelling ratio than the HCZ hydrogels. This suggests that the coordinate bond-mediated cross-linked hydrogels had a higher swelling ratio than the chemically cross-linked hydrogels. Compared to the HAZ hydrogel, the fraction of hydrophilic domains in HCZ hydrogels increased due to the presence of catechol-functionalized groups, thus allowing for the absorption of more water[27].

The in vitro degradation behavior was characterized by hyaluronidase, which is a specific enzyme that degrades HA, as shown in Fig. 3c. The degradation of hydrogels was determined by measuring the remaining weight at the given incubation time in the hyaluronidase solution. The enzymatic degradation rate of the HAZ hydrogel was considerably faster than that of the HCZ hydrogels. After 24 h of culturing in the enzyme solution at 37 °C, HAZ was fully degraded, whereas the remaining weights of HCZ 3, 5, and 10 were 47.4 ± 1.8, 73.8 ± 3.2, and

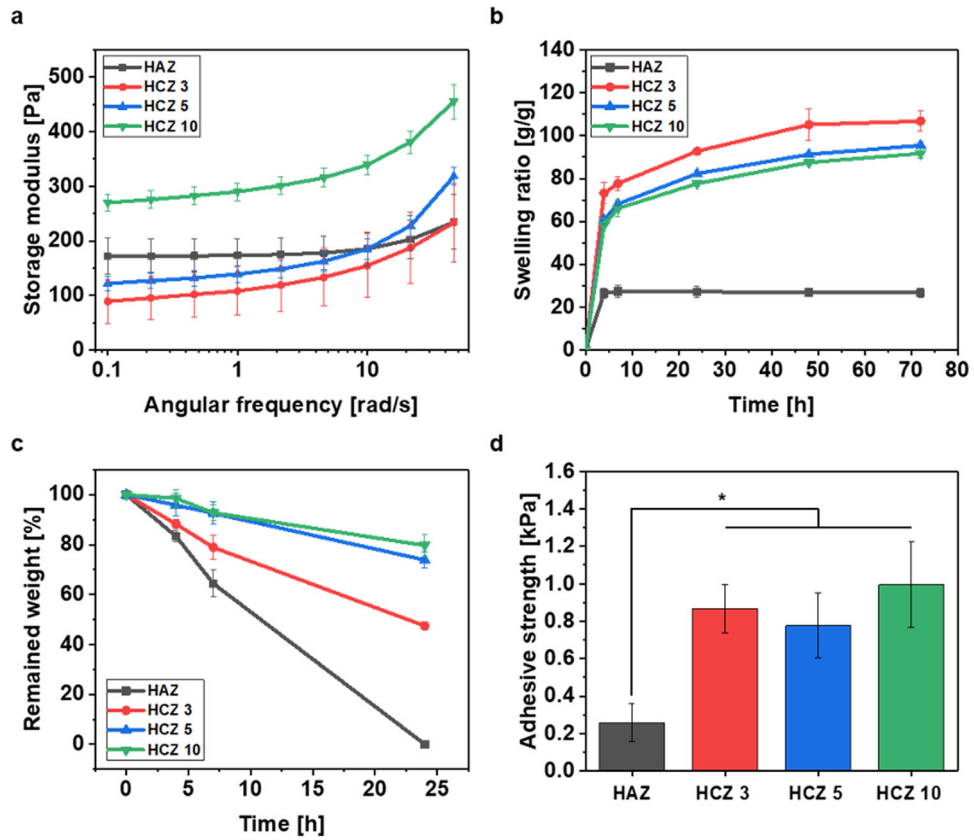

Fig. 3 Physical properties of HCZ hydrogels. a Rheological behavior measured from storage modulus for a frequency sweep mode. **b** Swelling ratio of the hydrogels for different time periods: 4, 7, 24, 48, and 72 h. **c** In vitro enzymatic degradation behaviors of the hydrogels in the presence of hyaluronidase. **d** Tissue adhesive strengths of the hydrogels calculated from lab shear strength. (*$p < 0.05$).

79.7 ± 4.6%, respectively. These results suggest that the catechol-ZnO coordination complex structure resisted enzymatic degradation better than the chemically cross-linked structure. Catechol-ZnO coordination complexes created multiple cross-linking points on the ZnO surface, which resulted in a delayed degradation rate. As the concentration of ZnO nanoparticles in the HCZ hydrogels increased, the remaining weight also increased due to the acquisition of more cross-linking points. Therefore, it is expected that catechol-ZnO coordination complexes could not only enhance the structural stability of HCZ hydrogels but also induce long-term therapeutic action under enzymatic degradation. The tissue adhesive strength of hydrogels was evaluated from the maximum shear stress recorded during the lab shear test, as illustrated in Fig. 3d. To compare the adhesive strength of the hydrogels themselves, the fabricated hydrogels were placed on the overlapping surface of porcine skins. The tissue adhesive strengths of HCZ hydrogels (0.87 ± 0.13 kPa for HCZ 3, 0.78 ± 0.17 kPa for HCZ 5, and 0.99 ± 0.23 kPa for HCZ 10) were considerably higher than that of the HAZ hydrogel (0.26 ± 0.1 kPa). The disparity in tissue adhesive strength between HCZ and HAZ hydrogels was attributed to the different cross-linking mechanisms. The catechol moiety in HCZ hydrogels has a high tissue adhesive capability due to versatile types of bonding with the surface, including hydrogen bonding. The concentration of functionalized catechol groups contributed to the tissue adhesive strength, which resulted in similar values between HCZ hydrogels regardless of the amount of ZnO nanoparticles.

Measurement of enhanced ROS generation

To inspect the free radical formation corresponding to the HCZ hydrogels, the EPR spectra of ZnO, HAZ, and HCZ are displayed in Fig. 4a. Two sharp signals at *g* values of 2.0037 and 1.96 were detected in all specimens, and these signals were assigned to radical species generated from the catechol-ZnO complexes and the singly ionized oxygen vacancies of ZnO nanoparticles, respectively[28,29]. The graph shape of HAZ was similar to that of ZnO, which suggests that HA cannot support the generation of more radicals after mixing with ZnO nanoparticles. However, the signal intensity of HCZ was extremely high

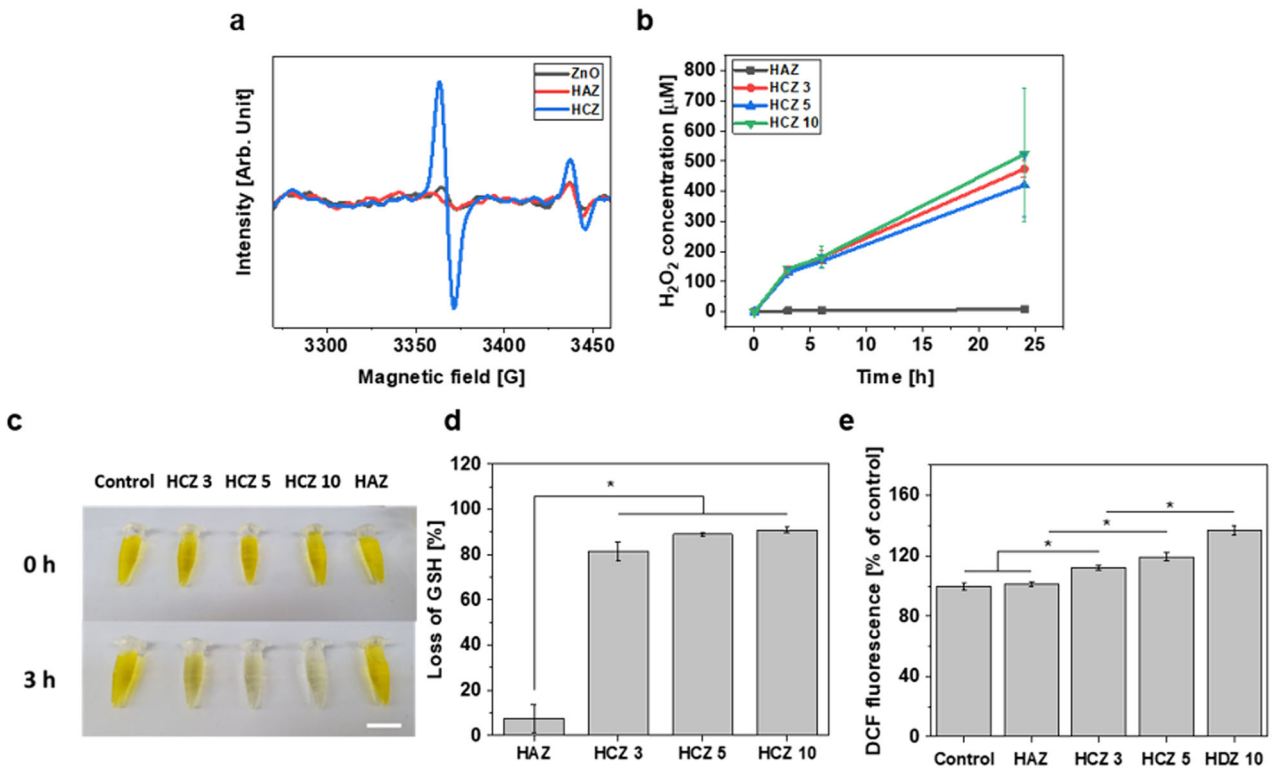

Fig. 4 Analysis of reactive oxygen species of the hydrogels. a Electron paramagnetic resonance (EPR) spectrum of ZnO, HAZ, and HCZ. **b** H_2O_2 concentrations generated from HAZ and HCZ hydrogels with different amounts of ZnO. **c** Optic images of color change of GSH after hydrogel immersion at 37 °C for 0 h and 3 h, respectively (scale bar: 2 cm). **d** Loss of GSH level after treating with hydrogels for 3 h. **e** The level of intracellular ROS generation in *S. aureus* after treatment with HAZ and HCZ hydrogels (*$p < 0.05$).

in both recognized peaks compared to other specimens. This could indicate that free radical generation was significantly increased during the coordination geometry formation of catechol-ZnO nanoparticles, which was attributed to o-semiquinone radicals and electron transfer from the oxidation of catechol[30]. Moreover, the catechol-ZnO coordination complex also triggered an increase in the intensity of the *g* value of 1.96, which was related to unpaired electron traps on oxygen vacancy defects[28].

The H_2O_2 concentration in the solution after treating the hydrogels was measured at each time interval, as shown in Fig. 4b. The colorimetric method was used to clarify the H_2O_2 concentration, which measured the absorbance after the color change. The HAZ hydrogel produced small amounts of H_2O_2, while the HCZ hydrogels could supply large amounts of H_2O_2 during the reaction with solution. This indicates that the radicals generated from the catechol-ZnO coordination complex convert water molecules into H_2O_2 species.

To further verify the oxidative stress induced by ROS released from HCZ hydrogels, the GSH depletion ability of the hydrogels was investigated. GSH is capable of protecting various cellular components by neutralizing ROS as it oxidizes into glutathione disulfide (GSSG)[31]. The depletion of GSH was quantitatively investigated with Ellman's assay to detect the remaining concentration of GSH after interacting with HCZ hydrogels. The control condition, with only GSH and HAZ hydrogel in the GSH solution, showed no color change after 3 h of immersion, whereas the color gradually became transparent in the presence of HCZ hydrogels (Fig. 4c). The loss of GSH was calculated based on the absorbance difference after exposure to the hydrogels, as shown in Fig. 4d. The HCZ hydrogels showed notably higher GSH oxidation ability (81.5% ± 4.0% for HCZ 3, 89.0% ± 0.5% for HCZ 5, and 90.9% ± 1.2% for HCZ 10) than the HAZ hydrogel (7.6% ± 6.2%). This indicates that ROS generation was crucially amplified by the formation of catechol-ZnO complexes in HCZ hydrogels.

In Fig. 4e, enhanced ROS generation was also demonstrated by the detection of intracellular ROS in *S. aureus*. The amount of intracellular ROS was defined based on the relative concentration of fluorescent 2′,7′-dichlorodihydrofluorescein (DCF). Compared to the control group, there was no significant increase in DCF intensity in HAZ. However, the fluorescence intensity of HCZ 3 was substantially enhanced although HCZ 3 and HAZ contained the same concentration of ZnO nanoparticles.

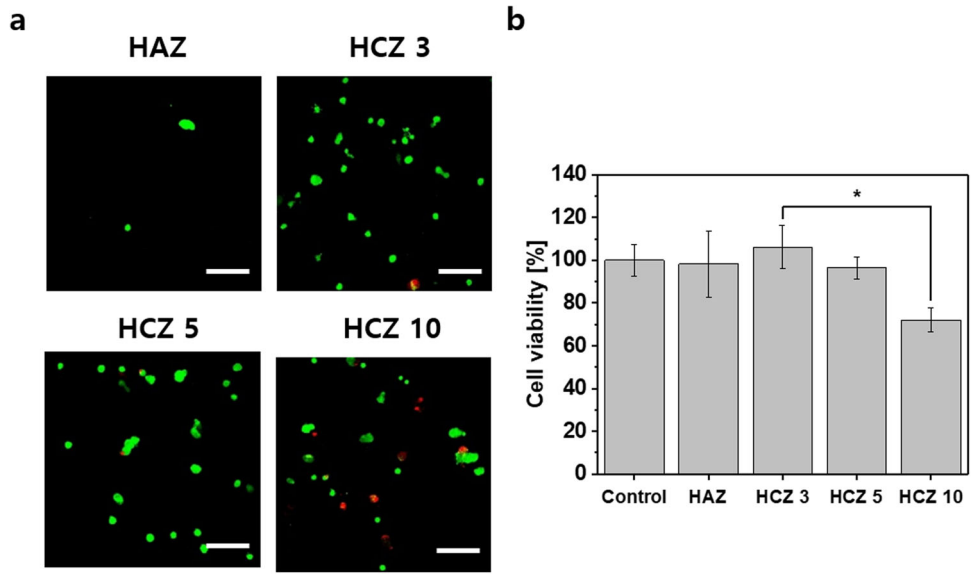

Fig. 5 In vitro cell tests of the hydrogels. a CLSM images of cultured HDF cells attached on HAZ and HCZ hydrogels. **b** Relative cell viability evaluation of HAZ and HCZ hydrogels after 24 h culturing in HDF cells (scale bar: 200 μm, *$p < 0.05$).

This indicates that the amount of intracellular ROS was increased by catechol-ZnO complexes, not ZnO nanoparticles themselves. In addition, as the concentration of ZnO nanoparticles in the hydrogel increased, intracellular ROS generation was further boosted because of the increased catechol-ZnO complex. These results strongly support the idea that HCZ hydrogels produce large amounts of ROS derived from the catechol-ZnO complex structure. We propose that the oxidation of catechol is catalyzed by ZnO nanoparticles in the process of catechol-ZnO complex formation, which induces electron transfer that transforms O_2 into $O_2^{\bullet-}$ and H_2O_2. Furthermore, *o*-semiquinone radicals generated from catechol oxidation could also affect the production of additional ROS.

In vitro cytocompatibility and antibacterial performance

The in vitro cytotoxicity of the hydrogels was inspected using fluorescence imaging and a WST-8 assay, which measures the cell viability. Figure 5a presents typical CLSM images of cell attachment on the hydrogels after 24 h of culturing. Few human dermal fibroblast (HDF) cells were attached to the surface of the HAZ hydrogel, whereas many cells firmly adhered to the HCZ hydrogels. This suggests that the catechol groups in HCZ hydrogels enhanced the biocompatibility of the hydrogels. In addition, no dead cells were observed in the hydrogels, except for HCZ 10, which showed a relatively large number of dead cells. The cell viability of the hydrogels is depicted in Fig. 5b, Figs. S8 and S9. As shown in Fig. S7, the antibacterial property of ZnO nanoparticles is related to the concentration. The numbers of Escherichia coli (*E. coli*) and Staphylococcus Aureus (*S. aureus*) decreased by an amount greater than the number of ZnO nanoparticles. It also revealed that HCZ hydrogels with high levels of ZnO nanoparticles have an antibacterial effect due to the toxicity of ZnO nanoparticles. To assess the cytotoxicity of the hydrogels, the samples were immersed in the media including a monolayer of cells for 24 h. Although no cytotoxicity was observed in HAZ, HCZ 3, and HCZ 5, the cell viability of cells cultured with HCZ 10 was slightly decreased due to the high density of ZnO nanoparticles. A sufficiently high concentration of ZnO nanoparticles decreased the cell viability, as depicted in Fig. S9.

The antibacterial properties of HCZ hydrogels were examined against two different bacterial strains, *E. coli* and *S. aureus*, which are representative of typical infectious bacteria. As shown in Fig. 6a, a disk diffusion test was conducted to identify the antibacterial efficacy of the hydrogels. No inhibition zone was observed in the HAZ hydrogel, while distinct inhibition zones were produced in HCZ 3, 5, and 10 for both bacterial strains. The bactericidal efficacy was also revealed by measuring the OD value at 595 nm after culturing both strains for 24 h, as shown in Fig. 6b. The OD value indicates the concentration of bacteria in the solution. The HAZ hydrogel showed weak antibacterial performance against *S. aureus*, which is attributed to the inherent antibacterial characteristics of ZnO nanoparticles. Compared to the HAZ hydrogel, the OD of both bacterial cultures was markedly decreased after exposure to the HCZ hydrogels. Although HAZ and HCZ 3 had the same amount of ZnO nanoparticles, HCZ 3 showed excellent antibacterial

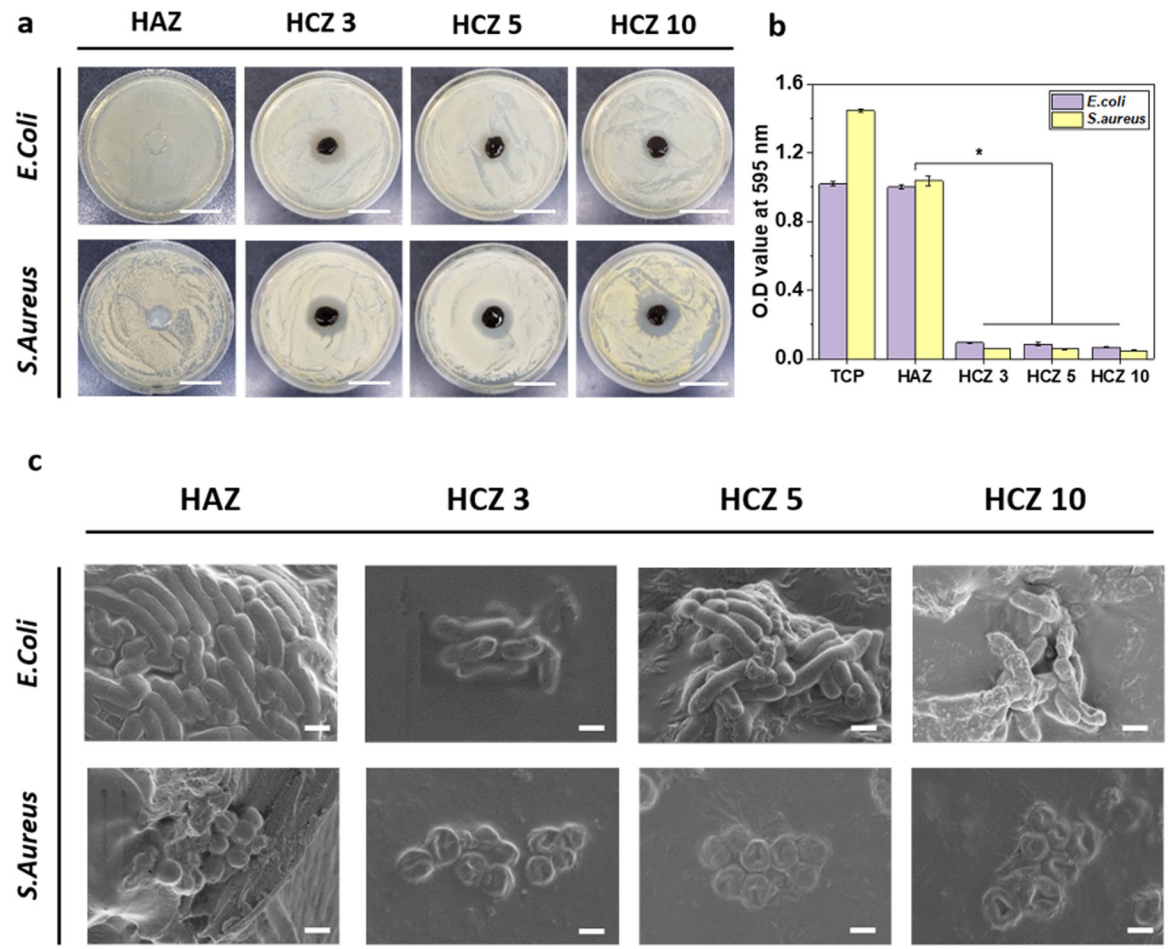

Fig. 6 In vitro antibacterial tests of the hydrogels. a Disk diffusion test images against *E. coli* and *S. aureus* of HAZ and HCZ hydrogels (scale bar: 20 mm). b Bactericidal efficacies of hydrogels against both bacteria strain after 24 h incubation (*$p < 0.05$). **c** Morphologies of *E. coli* and *S. aureus* attached on the surface of the hydrogels (scale bar: 1 μm).

properties. These results were consistent with the results of the disk diffusion test, which corroborated the antibacterial property of HCZ hydrogels. Hence, the morphology of bacteria exposed to hydrogels demonstrated the antibacterial activity of HCZ hydrogels (Fig. 6c). No deformation of the bacterial structure was recognized in the HAZ hydrogel, while the membranes of both bacterial strains were ruptured after culturing on HCZ hydrogels. These results were attributed to the high concentration of ROS released from HCZ hydrogels, which is the major factor in effectively killing the two bacterial strains. Excessive ROS generation produces enormous amounts of oxidative stress, which in turn induces membrane disruption and DNA damage in bacterial cells through the peroxidation of unsaturated phospholipids[32].

In vivo antibacterial performance

To further investigate the antibacterial performance of HCZ hydrogels, an in vivo bacterial infection model was constructed using *S. aureus*. The inoculated bacteria and injected hydrogels were observed after harvesting the infected tissues, and the results are shown in Fig. 7a and Fig. S10. Colony formation tests confirmed the enhanced antibacterial properties of HCZ hydrogels (Fig. 7b). Tissues treated with PBS were used as the negative control. In the case of HAZ hydrogel, the number of colonies was not decreased compared to the control, which indicated that it had less effective antibacterial properties despite containing ZnO nanoparticles. However, the number of bacterial colonies was drastically decreased (by ~4 times) through treatment with the HCZ 3 and HCZ 10 hydrogels, as shown in Fig. 7c. In particular, the HCZ 3 hydrogel revealed excellent antibacterial performance despite the presence of the same concentration of ZnO nanoparticles as the HAZ hydrogel. Although HCZ 10 showed results similar to those of HCZ 3, HCZ 3 was the best candidate for antibacterial therapy due to its better biocompatibility with cells than HCZ 10, as described in Fig. 5. In addition,

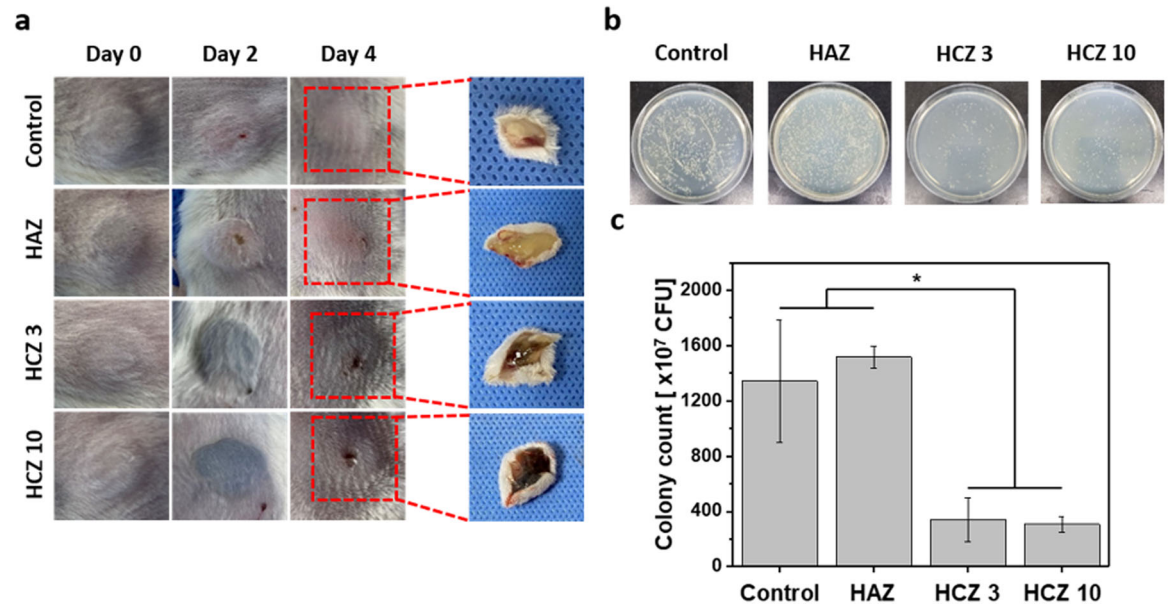

Fig. 7 In vivo observation. a Representative photographs of skin lesions infected with *S. aureus* on days 0, 2, and 4 for each group. **b** In vivo antibacterial efficacy test images for each group and c the count of *S. aureus* colonies (*$p < 0.05$).

since HCZ 3 has moderate degradability, it is considered ideal since it will moderately degrade after ROS release, as depicted in Fig. 3c.

This suggests that catechol-ZnO complexes contribute to the increased antibacterial capability, as opposed to the ZnO nanoparticle itself. Figure 8a shows H&E histological section images of each specimen, which clearly show many inflammatory cells in the infected sites. The abscess area, bacterial band length, and cellularity were calculated from the H&E histological images to quantitatively determine the antibacterial performance. The abscess area and bacterial band length of HCZ 3 and HCZ 10 were reduced compared to those of the control and HAZ groups, and HCZ 10 in particular showed a significantly diminished abscess area (Fig. 8b, c).

The bacterial cellularity showed a similar tendency as the other quantitative figures, which confirms that HCZ 3 and HCZ 10 had decreased abundance of inflammatory cells, as detailed in Fig. 8d. Since white blood cell (WBC) and neutrophil counts are generally known as sensitive and reliable indicators of inflammatory activity[33], additional in vivo hematological analysis was performed. At the time of sacrifice, we conducted analysis of peripheral blood profiles. As shown in Fig. 9a, the proportions of WBCs and neutrophils in whole blood were considerably reduced with HCZ 10 treatment. The absolute WBC and neutrophil counts were also significantly decreased with HCZ 10 treatment (Fig. 9b, c). We also measured serum C-reactive protein (CRP), which is an acute-phase protein that is highly expressed in inflammation and tissue damage[34]. Compared to the control groups, serum CRP levels in infected mice were observed to be slightly lower in the case of HCZ 3 and significantly lower in the regulated HCZ 10 groups (Fig. 9d). Altogether, the results of histological and hematological analyses demonstrate that HCZ hydrogels have effective antibacterial properties. Furthermore, the antibacterial performance of HCZ hydrogels was substantially improved with increasing ZnO nanoparticle concentration.

Conclusions

In summary, we have successfully developed a hyaluronic acid hydrogel platform via catechol-ZnO complexes that can deliver enhanced antibacterial therapy. The hydrogel system was fabricated via reversible coordinate bonds that cross-link catechol moieties and ZnO nanoparticles. This hydrogel showed higher tissue adhesion than the HAZ hydrogel due to the anchoring ability of functionalized catechol moieties in the hydrogel matrix, which facilitates the release of ROS at the appropriate inflammatory site. Notably, the hydrogel is injectable, tissue adhesive, and biodegradable; thus, it is possible to intensively treat localized infections by injecting directly into the area to be treated and it will adhere to the tissue. Because it is biodegradable, it can be said to be an ideal antibacterial treatment. In this study, tissue adhesion refers to adhesivity to the extent that it can localize without flowing because it adheres well to the skin after injection. Due to the generation of ROS during the formation of the catechol-ZnO complex, this hydrogel

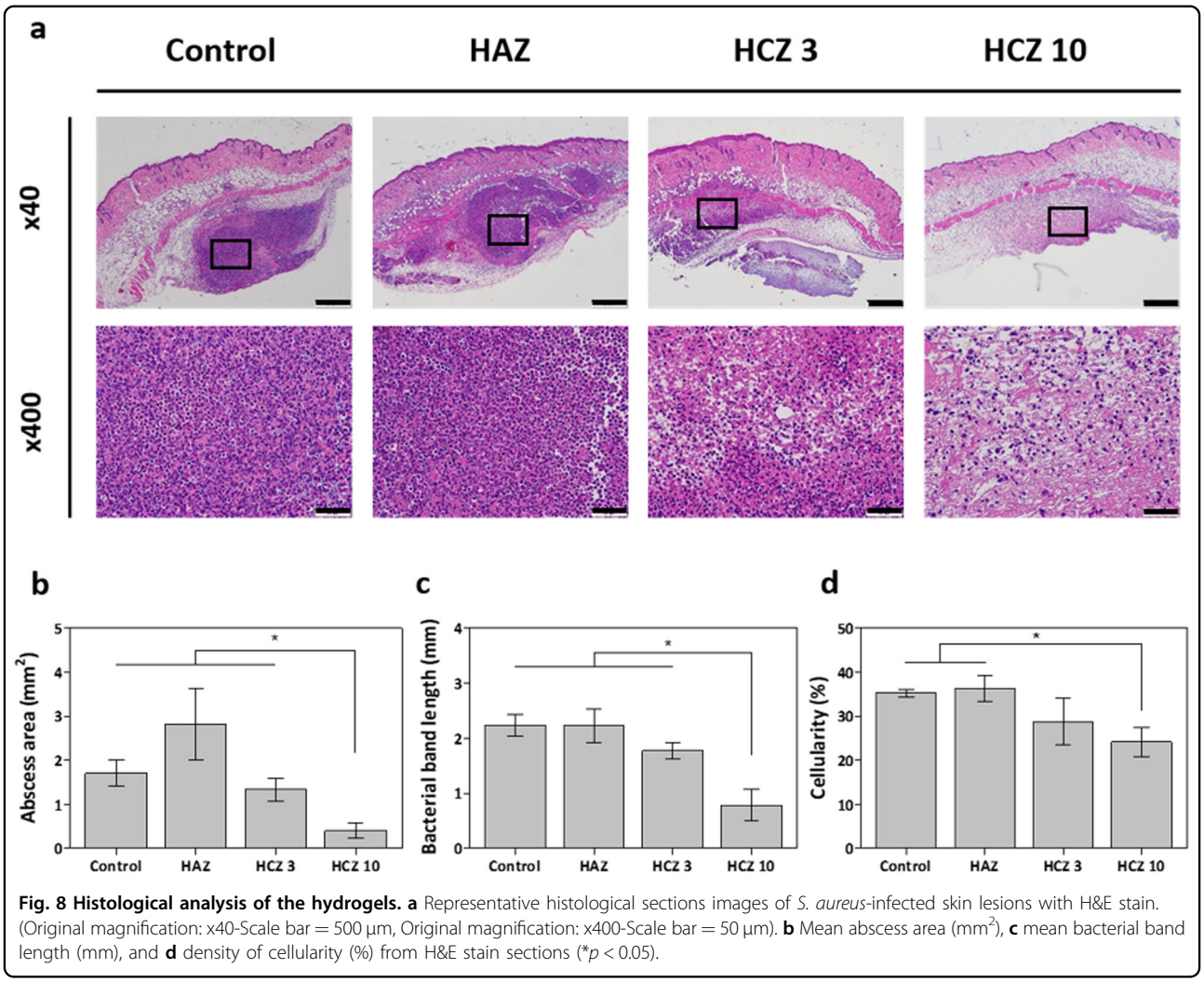

Fig. 8 Histological analysis of the hydrogels. a Representative histological sections images of *S. aureus*-infected skin lesions with H&E stain. (Original magnification: x40-Scale bar = 500 μm, Original magnification: x400-Scale bar = 50 μm). **b** Mean abscess area (mm^2), **c** mean bacterial band length (mm), and **d** density of cellularity (%) from H&E stain sections (*$p < 0.05$).

platform showed enhanced ROS generation as well as outstanding antibacterial performance against both *E. coli* and *S. aureus* compared to HAZ. In addition, a mouse full-thickness *S. aureus* infection model also showed that HCZ hydrogels had remarkable potential to eradicate bacteria. This work presents a new approach to the design of a hydrogel platform that self-generates ROS for enhanced antibacterial therapy. The HCZ hydrogel could be applied to the treatment of clinically chronic wound sites by introducing effective antibacterial properties for open wounds. It could also be applied as an antibacterial coating material for biomedical devices as well as used in closed subcutaneous spaces. Finally, with improved adhesion, the HCZ hydrogel could act as a dressing material for wounded areas.

Materials and methods

Materials

HA sodium salt (molecular weight of 50–110 kDa) was purchased from Pharmaline Co. (Suwon, Korea). Zinc acetate dihydrate (99.999% trace metals basis), sodium periodate, methanol, dopamine hydrochloride, 1-ethyl-3-(3-demethylaminopropyl)carbodiimide hydrochloride (EDC), N-hydroxysuccinimide (NHS), 1,4-butanediol diglycidyl ether (BDDE), dialysis tubing cellulose membrane (molecular weight cut off = 14,000), 5,5-dithio-bis-(2-nitrobenzoic acid) (DTNB), reduced L-glutathione, and hyaluronidase (Type I-S, lyophilized powder, 400–1000 units/mg solid) were all purchased from Sigma Aldrich (St. Louis, USA).

Synthesis and characterization of HA-CA

HA-CA was synthesized using EDC/NHS coupling agents wherein the carboxyl groups of the HA chain were reacted with the amine groups of dopamine. Briefly, 2 g of HA was dispersed in 100 ml of PBS, and the pH value of the solution was adjusted to 5.5 using 1 M hydrochloric acid (HCl). Next, EDC, NHS, and dopamine hydrochloride (DA) were added to the HA solution. The final molar concentration ratio of HA/EDC/NHS/DA was 1:1:1:1, and the mixed solution was

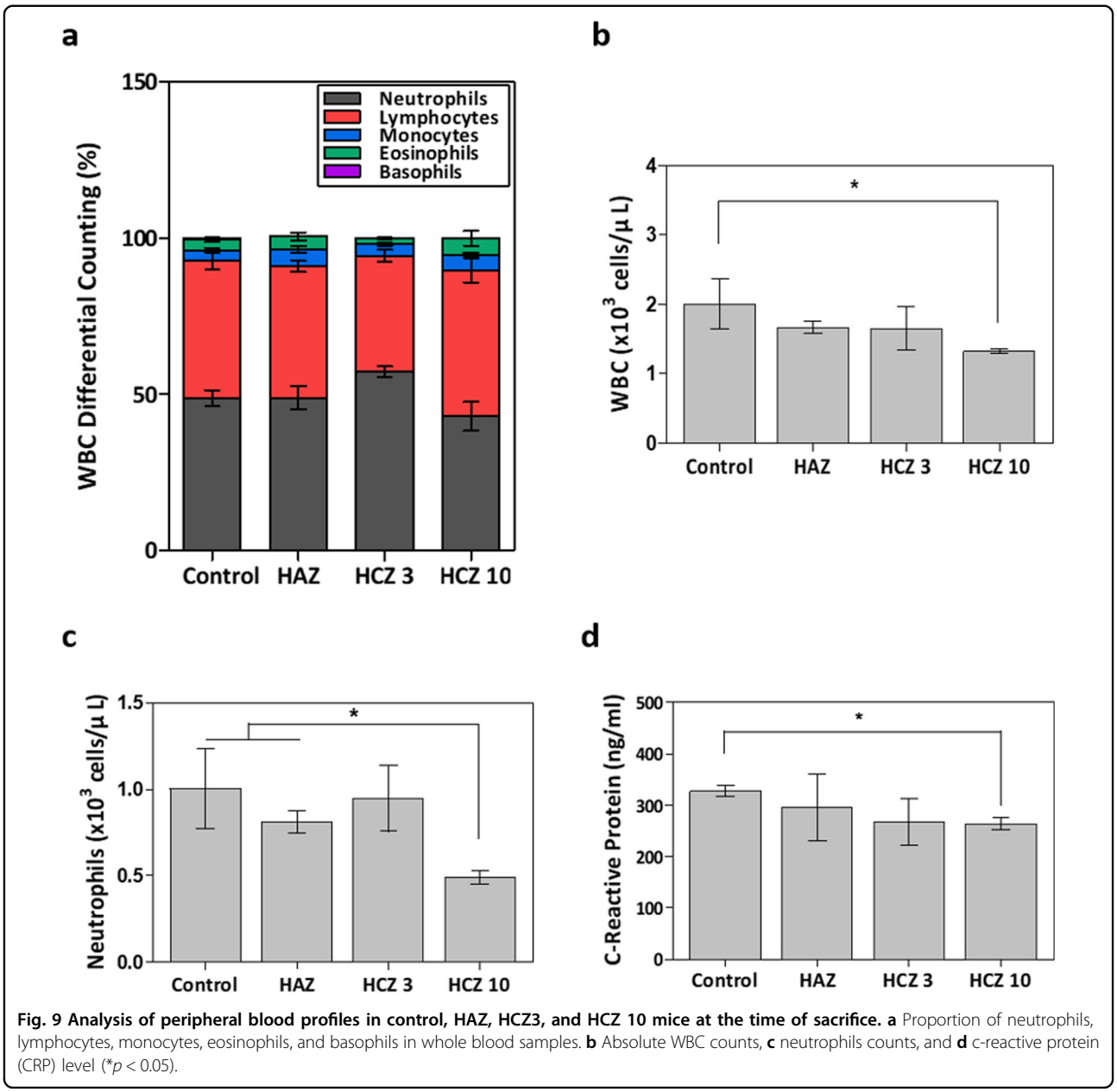

Fig. 9 Analysis of peripheral blood profiles in control, HAZ, HCZ3, and HCZ 10 mice at the time of sacrifice. a Proportion of neutrophils, lymphocytes, monocytes, eosinophils, and basophils in whole blood samples. **b** Absolute WBC counts, **c** neutrophils counts, and **d** c-reactive protein (CRP) level (*$p < 0.05$).

maintained overnight at room temperature. Following the reaction, to remove unreacted dopamine, dialysis was conducted for 2 days in pH 5.5 PBS solution and 4 h in distilled water, followed by lyophilization. Synthesized HA-CA was stored at 4 °C until used in the experiment. The conjugated catechol groups in HA-CA were confirmed using ^{1}H-nuclear magnetic resonance (NMR) (Avance III-500, Brucker, Germany), and the substituted catechol ratio of HA-CA was determined by detecting the absorbance at 280 nm using UV–vis spectroscopy (V-770, JASCO, USA) with a dopamine standard curve.

Preparation of ZnO nanoparticles

ZnO nanoparticles were fabricated by a precipitation method from a zinc acetate precursor. Briefly, 0.1 M zinc acetate dihydrate solution was prepared using methanol as a solvent. Next, 1 M sodium hydroxide solution was dropped into the prepared zinc acetate solution under vigorous stirring for 1 h. The precipitated ZnO nanoparticles were then obtained by centrifugation and washed several times using ethanol and distilled water. Finally, after drying the ZnO powders at 70 °C, calcination was conducted at 500 °C for 1 h.

Fabrication of HCZ hydrogel samples

For each hydrogel specimen, the ZnO nanoparticles were dispersed in distilled water and then sonicated for 1 h. After sonication, 5 wt% HA-CA was dissolved into the ZnO solution, and it was stirred until the polymer was fully dissolved. The concentrations of ZnO nanoparticles in the mixed solution were determined to be 3, 5, and 10 wt% of the amount of HA-CA. The mixed solution was transferred into a plastic mold, and the HCZ hydrogels were prepared after being placed at 50 °C for 24 h. The HAZ hydrogel was fabricated by a chemical cross-linking system using BDDE including HA and ZnO nanoparticles: 5 wt% HA in 0.2 M NaOH was combined with 3 wt% ZnO nanoparticles under stirring and then mixed with 80 μl/ml BDDE. The HAZ hydrogel was allowed to polymerize at 37 °C for 24 h.

Characterization of hydrogels

The morphologies of the HAZ and HCZ hydrogels were observed using field emission scanning electron microscopy (FE-SEM, SUPRA SSVP, Carl Zeiss Inc., Germany). Before observation, the hydrogels were prepared by lyophilization, followed by coating with platinum for electrical conduction. ZnO nanoparticles were analyzed using transmission electron microscopy (TEM, JEM-2100F, JEOL Ltd., Japan) with an accelerating voltage of 200 kV to identify the structure. The phase of the ZnO nanoparticles in the hydrogel was determined by an X-ray diffraction (XRD; D8-Advance, Brucker Co., Germany) with a scanning range of 20°−80° at a rate of 1°/min. The chemical structures of the coatings were identified by attenuated total reflectance Fourier transform infrared spectroscopy (FT-IR, Nicolet 6700, Thermo Scientific, USA) for wavenumbers ranging from 600 to 4000 cm^{-1} with an average of 32 scans. X-ray photoelectron spectroscopy (XPS, AXIS SUPRA, Kratos, UK) was conducted using monochromatic Al K_α radiation to confirm the chemical states of the composing elements of HCZ. To observe the XPS peaks, dried hydrogels were prepared through lyophilization. UV−visible light absorption spectra were characterized using UV−visible spectroscopy (V-770, JASCO, Japan) ranging from 260 to 800 nm. The zeta potential and particle size distribution were measured by dynamic light scattering (DLS, ELSZ 1000ZS size and zeta potential analyzer, Japan). The zeta potential and hydrodynamic diameter were obtained from a 50-fold diluted HA-CA solution containing ZnO nanoparticles. Electron paramagnetic resonance (EPR) measurements were conducted on an EPR spectrometer (EMXmicro-9.5/2.7, Bruker Co., Germany) at the X-band frequency (9.43 GHz). To verify the radical formation in the system, a mixed solution containing 20 mg/ml ZnO nanoparticles and 10 mg/ml HA and HA-CA polymer was used. Then, baseline correction processing of the acquired spectra was performed using WinEPR process software (Bruker, USA).

Swelling and degradation behavior

The equilibrium swelling ratio of HAZ and HCZ hydrogels was confirmed in PBS solution at 37 °C for each time point. Before swelling, the hydrogels were dried by lyophilization to obtain the initial weight (W_i). At certain time points, the weights of the hydrogels were measured after removing the buffer solution on the hydrogel surface. The swelling ratio of the hydrogels was calculated as

$$\text{Swelling ratio (g/g)} = (W - W_i)/W_i$$

where W_i and W are the weights of the dried hydrogels and swollen hydrogels, respectively.

In vitro enzymatic degradation behavior was observed in PBS solution containing hyaluronidase at a concentration of 12.5 μg/mL (5–12.5 UI/mL) at 37 °C. The initial weight (W_i) was determined after 1 day of swelling in PBS solution, while the remaining weight (W_r) was measured at certain time intervals in PBS with hyaluronidase solution. The remaining weight ratio was calculated using the following equation:

$$\text{Remaining weight ratio (\%)} = (W_r/W_i) \times 100$$

Rheological behavior

The rheological behavior of the hydrogels was examined using the frequency sweep mode of a rheometer (TA). All specimens were fabricated with a diameter of 20 mm and a thickness of 2 mm. The storage modulus (G′) and loss modulus (G″) were confirmed under a constant strain (0.01) over the frequency range from 0.1 to 50 rad/s with 20 mm diameter parallel plates.

Tissue adhesion strength

The tissue adhesion strengths of HAZ and HCZ hydrogels were measured using a universal testing machine (Instron 5543, Instron, USA) with a 50 N load cell to obtain the adhesive strength between hydrogels and porcine skin; porcine skins were purchased from a local slaughterhouse. Porcine skins were cut into 10 mm × 30 mm pieces and immersed in PBS buffer at 37 °C for 3 h to maintain the hydrate state. Hydrated porcine skins were attached to clear cover glass using cyanoacrylate glue (Loctite, Germany). The fabricated hydrogel samples were prepared with an area of 10 mm × 10 mm and deposited between two porcine skin substrates. Subsequently, the tissue adhesion strength was tested by a lab shear test method under a cross-head speed of 3 mm/min. The adhesion strengths of the hydrogels were calculated as the maximum tensile strength divided by the joint area.

In vitro antibacterial performance of hydrogels

To evaluate the antibacterial activity of the hydrogels, two bacterial strains, *Escherichia coli* (*E. coli*, ATCC 8739, gram-negative) and *Staphylococcus aureus* (*S. aureus*, ATCC 6538, gram-positive), were evaluated when cultured with the hydrogels through an agar diffusion test and an optical density (OD) value test at 595 nm. Fifty microliters of *E. coli* and *S. aureus* were inoculated in 3 ml of fresh Luria-Bertani (LB) broth (BD DifcoTM, 244620, USA), followed by culturing overnight at 37 °C in a shaker at 200 rpm. To measure the OD value at 595 nm, 200 µl, and 50 µl of the prepared hydrogels were placed into the diluted *E. coli* and *S. aureus* solution, which had a concentration of 5×10^4 CFU/ml, in a 12-well culture plate, and then each solution was cultured at 37 °C for 24 h. Next, 200 µl of the treated bacterial suspension was collected in a 96-well culture plate, and the OD value at 595 nm was collected. For the agar diffusion test, 200 µl of diluted bacterial suspension was dropped and spread on the agar plate using a triangular bar. Two hundred microliters of the prepared hydrogels was located on the center of the agar plate and then incubated at 37 °C for 24 h. The images of the inhibition zone were acquired using a digital camera. The morphological changes in the bacteria were observed using FE-SEM on the surface of the hydrogels. The hydrogels were covered with 1×10^7 CFU/ml of both bacterial strain solutions at 37 °C for 3 h. The bacteria attached to the hydrogels were fixed with 2.5% glutaraldehyde for 10 min and then dehydrated in 75%, 95%, and 100% ethanol for 5 min each. Then, the samples were placed in hexamethyldisilazane for 10 min twice before being air dried.

Intracellular reactive oxygen species (ROS) detection

Levels of intracellular ROS generation were detected using 2′,7′-dichlorofluorescin diacetate (DCFDA, Assaygenie, UK), which transforms into a fluorescent dye after diffusion into the cells. First, 50 µl of *S. aureus* was inoculated overnight in 3 ml of fresh Luria-Bertani (LB) broth (BD DifcoTM, 244620, USA) at 37 °C in a shaker. Suspended *S. aureus* was collected by centrifugation at 4000 rpm, washed with PBS twice, and then exposed to 25 µM DCFDA for 45 min. Next, hydrogels were immersed into diluted *S. aureus* solution at a concentration of 1×10^7 CFU/ml for 3 h in the dark. Finally, the fluorescence intensity was recorded by the excitation of a 485 nm laser and the emission of a 535/20 nm filter using a microplate reader (Victor 3, Perkin Elmer, USA). The fluorescence intensity is proportional to the amount of intracellular ROS.

Oxidative stress measurement via glutathione (GSH) depletion

To monitor the level of oxidative stress by ROS generation from hydrogels, GSH depletion was measured by quantifying the concentration of thiol groups after interacting with hydrogels using Ellman's assay[35]. Typically, 200 µl of hydrogels was immersed in 3 ml of GSH bicarbonate buffer solution (GSH, 1 mM; bicarbonate buffer, 50 mM, pH = 8.7). After 3 h of incubation at 37 °C, 50 µl of bicarbonate buffer solution with DTNB (10 mM) was dropped into the GSH solution. The reacted solution was then collected to measure the absorbance at 412 nm. The loss of GSH was calculated as follows: Loss of GSH [%] = (absorbance of negative control − absorbance of sample)/absorbance of negative control × 100. The negative control was GSH solution without any samples.

H_2O_2 generation measurement

To determine the concentration of H_2O_2 generated from HCZ hydrogels, the amount of H_2O_2 was quantified using a Quantitative Peroxide Assay Kit (Pierce, Rockford, USA). Briefly, 200 µl of the hydrogels was immersed in 3 ml of PBS solution for predetermined time intervals (3 h, 6 h, and 24 h). Next, 20 µl of each treated medium was added to 200 µl of assay kit reagent and incubated at room temperature for 20 min. The absorbance was measured at 595 nm on a microplate reader (EZ read 400, Biochrom, UK). The standard curve of H_2O_2 concentration was obtained from 30% H_2O_2 solution diluted to 100–1000 µM.

In vitro cytotoxicity

In vitro cytotoxicity tests were performed by measuring the cell attachment and viability of the hydrogels using human dermal fibroblasts (HDFs, ATCC® PCS-201-012™). The cells were cultured in alpha minimum essential medium (α-MEM, Welgene, Korea) containing 10% fetal bovine serum (Gibco, USA) and 1% penicillin–streptomycin (Pen strep, Gibco, USA) in an incubator at 37 °C under 5% CO_2. To observe cell attachment, the cells (5×10^4 cells/mL) were seeded onto the hydrogels on a 4-well culture plate. After culturing for 24 h, the samples were stained with green-fluorescent calcein AM (Thermo Scientific, USA) for 30 min so that the morphology of the attached cells could be observed using a confocal laser scanning microscope (CLSM, LSM710, Carl Zeiss, Germany).

Cell viability was assessed using a WST-8 cell viability assay (Quanti-Max™, Biomax, Korea). The cells were suspended in a 24-well culture plate at a density of 1×10^4 cells/mL with incubation for 24 h at 37 °C, after which the hydrogels were placed in the solution for 24 h. Then, the cell culture medium was substituted with 10% WST-8 solution and cultured for 2 h. The obtained formazan products in the reactant were analyzed at an absorbance of 450 nm using a microplate reader (EZ read 400, Biochrom, UK). The cell viability was represented as a percentage of the tissue culture plate area.

In vivo antibacterial experiment

The in vivo study was approved by the Institutional Biosafety Committee (IBC) and Institutional Care and Use Committee (IACUC) of Seoul National University (IBC number SNUIBC-R210202-1 and IACUC number SNU-210319-2). BALB/c male mice (5 weeks, $n = 5$) were purchased from OrientBio (Gapyeong, Korea). All animal experiments were conducted according to the Seoul National University IACUC guidelines.

To evaluate the antibacterial properties of HCZ hydrogels, bacterial infection was initiated in the subcutaneous skin tissue of BALB/c mice. The dorsal hair of the mice was removed, and the subcutaneous skin was inoculated with 100 µl of *S. aureus* (OD = 1). After inoculation for 48 h, 100 µl of PBS, HAZ, HCZ 3, or HCZ 10 was injected into the infected tissue. After 2 days, the mice were sacrificed to harvest the treated tissues. For colony formation testing, the infected tissues were ground and diluted in PBS solution. Next, 200 µl of diluted suspension was placed and cultured on LB agar plates for 24 h at 37 °C. Colony formation images were obtained using a digital camera, and the number of colonies formed was counted using ImageJ software. For histological analysis, the infected tissues were collected and fixed in paraformaldehyde solution (4%). The paraffin blocks were fabricated and sectioned (4 µm), and histological images were obtained using hematoxylin and eosin (H&E, ab245880, Abcam, UK). The abscess area was calculated using the following equation[36,37]:

$$\text{Abscesses area}\left(\text{mm}^2\right) = \text{long dimension} * \text{short dimension}$$

The bacterial band length (measuring both edges from the center of the abscess[36], ×40 magnification) and the cellularity (×400 magnification) in the H&E-stained sections were determined for each section using a microscope (BX53, Olympus Corporation, Japan). For peripheral blood profiles, whole blood samples were collected for each group at the time of sacrifice. An automatic hematology analyzer (XN-1000, SYSMEX, Japan) was used to perform the white blood cell counts. To measure the C-reactive protein (CRP) level, serum isolated from whole blood was measured using an enzyme-linked immunosorbent assay kit (ELISA, ab157712, Abcam).

Statistical analysis

All experimental results were statistically represented as the means ± standard deviations[38]. The Statistical Package for the Social Sciences (SPSS, IBM, USA) was used to analyze the difference between specimens. The normality of the variables was evaluated using one-way analysis of variance (ANOVA) and Tukey's post hoc analysis. A p value below 0.05 was considered to be significant in all cases.

In the in vivo experimental results, all statistical values were reported as the means ± standard errors of the means. The statistical tests were evaluated by the Mann–Whitney nonparametric U test, and multiple comparisons were tested with two-way analysis of variance using GraphPad Prism 5.0 software. A p value <0.05 was considered to be statistically significant.

Acknowledgements

C.-H.H. and S.-H.J. conceived the idea and developed the materials and methods for the hydrogels. C.-H.H. designed and carried out the experiments, including synthesis, characterization, and in vitro tests. M.-H.C. and J.-U.P. contributed to the performance of the in vivo animal experiment and analysis. C.-H.H. wrote the main manuscript. S.-H.J. supervised this study and provided intellectual guidance. All authors discussed the results and commented on the manuscript. This study was supported by the Korea Medical Device Development Fund grant funded by the Korean government (the Ministry of Science and ICT, the Ministry of Trade, Industry and Energy, the Ministry of Health & Welfare, Republic of Korea, the Ministry of Food and Drug Safety) (0581-20210022) and a focused clinical research grant-in-aid from the Seoul Metropolitan Government Seoul National University (SMG-SNU) Boramae Medical Center (04-2021-0006). This work was supported by the Korea Medical Device Development Fund grant funded by the Korean government (the Ministry of Science and ICT, the Ministry of Trade, Industry and Energy, the Ministry of Health & Welfare, Republic of Korea, the Ministry of Food and Drug Safety) (Project Number: 202011B29).

Author details

[1]Department of Materials Science and Engineering, Seoul National University, Seoul 08826, Republic of Korea. [2]Department of Plastic and Reconstructive Surgery, Seoul National University Boramae Medical Center, Seoul National University College of Medicine, Seoul 07061, Republic of Korea. [3]Advanced Institutes of Convergence Technology, Seoul National University, Gwanggyo, Yeongtong-gu, Suwon-si, Gyeonggi-do 16229, Republic of Korea

Conflict of interest

The authors declare no competing interests.

Supplementary information The online version contains supplementary material available at https://doi.org/10.1038/s41427-022-00420-5.

Received: 3 February 2022 Revised: 4 June 2022 Accepted: 4 July 2022.
Published online: 19 August 2022

References

1. Wang, Y. et al. Photothermal conversion-coordinated Fenton-like and photocatalytic reactions of $Cu_{2-x}Se$-Au Janus nanoparticles for tri-combination antitumor therapy. *Biomaterials* **255**, 120167 (2020).
2. Sivakumar, P., Lee, M., Kim, Y.-S. & Shim, M. S. Photo-triggered antibacterial and anticancer activities of zinc oxide nanoparticles. *J. Mater. Chem. B* **6**, 4852–4871 (2018).
3. Quinones, R. et al. Study of perfluorophosphonic acid surface modifications on zinc oxide nanoparticles. *Materials* **10**, 1363 (2017).
4. Lakshmi Prasanna, V. & Vijayaraghavan, R. Insight into the mechanism of antibacterial activity of ZnO: surface defects mediated reactive oxygen species even in the dark. *Langmuir* **31**, 9155–9162 (2015).
5. Kumar, S. et al. Efficient electron transfer across a ZnO-MoS_2-reduced graphene oxide heterojunction for enhanced sunlight-driven photocatalytic hydrogen evolution. *ChemSusChem* **10**, 3588–3603 (2017).

6. Wang, S. et al. Enhanced antitumor efficacy by a cascade of reactive oxygen species generation and drug release. *Angew. Chem. Int. Ed. Engl.* **58**, 14758–14763 (2019).
7. Wiesmann, N., Tremel, W. & Brieger, J. Zinc oxide nanoparticles for therapeutic purposes in cancer medicine. *J. Mater. Chem. B* **8**, 4973–4989 (2020).
8. Zhang, Y., Nayak, T. R., Hong, H. & Cai, W. Biomedical applications of zinc oxide nanomaterials. *Curr. Mol. Med.* **13**, 1633–1645 (2013).
9. Saravanan, R. et al. Enhanced photocatalytic activity of ZnO/CuO nanocomposite for the degradation of textile dye on visible light illumination. *Mater. Sci. Eng. C. Mater. Biol. Appl.* **33**, 91–98 (2013).
10. Yi, G., Li, X., Yuan, Y. & Zhang, Y. Redox active Zn/ZnO duo generating superoxide ($^{\cdot}O^{2-}$) and H_2O_2 under all conditions for environmental sanitation. *Environ. Sci.: Nano* **6**, 68–74 (2019).
11. Ancona, A. et al. Lipid-coated zinc oxide nanoparticles as innovative ROS-generators for photodynamic therapy in cancer cells. *Nanomaterials* **8**, 143 (2018).
12. Hong, S. et al. Hyaluronic acid catechol: a biopolymer exhibiting a pH-dependent adhesive or cohesive property for human neural stem cell engineering. *Adv. Funct. Mater.* **23**, 1774–1780 (2013).
13. Black, K. C., Liu, Z. & Messersmith, P. B. Catechol redox induced formation of metal core-polymer shell nanoparticles. *Chem. Mater.* **23**, 1130–1135 (2011).
14. Park, H. J. et al. Catechol-functionalized hyaluronic acid hydrogels enhance angiogenesis and osteogenesis of human adipose-derived stem cells in critical tissue defects. *Biomacromolecules* **17**, 1939–1948 (2016).
15. Amstad, E., Gillich, T., Bilecka, I., Textor, M. & Reimhult, E. Ultrastable iron oxide nanoparticle colloidal suspensions using dispersants with catechol-derived anchor groups. *Nano Lett.* **9**, 4042–4048 (2009).
16. Li, Q., Barrett, D. G., Messersmith, P. B. & Holten-Andersen, N. Controlling hydrogel mechanics via bio-inspired polymer-nanoparticle bond dynamics. *ACS Nano* **10**, 1317–1324 (2016).
17. Kord Forooshani, P. et al. Hydroxyl radical generation through the Fenton-like reaction of hematin- and catechol-functionalized microgels. *Chem. Mater.* **32**, 8182–8194 (2020).
18. Yang, J., Cohen Stuart, M. A. & Kamperman, M. Jack of all trades: versatile catechol crosslinking mechanisms. *Chem. Soc. Rev.* **43**, 8271–8298 (2014).
19. Zhang, Z. et al. Iron magnetic nanoparticle-induced ROS generation from catechol-containing microgel for environmental and biomedical applications. *ACS Appl. Mater. Interfaces* **12**, 21210–21220 (2020).
20. Lu, X. et al. Magnesium oxide-crosslinked low-swelling citrate-based mussel-inspired tissue adhesives. *Biomaterials* **232**, 119719 (2020).
21. Jeong, S. H. et al. Strong and biostable hyaluronic acid-calcium phosphate nanocomposite hydrogel via in situ precipitation process. *Biomacromolecules* **17**, 841–851 (2016).
22. Guo, Z., Mi, S. & Sun, W. The multifaceted nature of catechol chemistry: bioinspired pH-initiated hyaluronic acid hydrogels with tunable cohesive and adhesive properties. *J. Mater. Chem. B* **6**, 6234–6244 (2018).
23. Neto, A. I. et al. Nanostructured polymeric coatings based on chitosan and dopamine-modified hyaluronic acid for biomedical applications. *Small* **10**, 2459–2469 (2014).
24. Zak, A. K., Razali, R., Majid, W. H. & Darroudi, M. Synthesis and characterization of a narrow size distribution of zinc oxide nanoparticles. *Int. J. Nanomed.* **6**, 1399–1403 (2011).
25. Burger, A., Srikantharajah, R., Peukert, W. & Hirsch, A. Individualization and stabilization of zinc oxide nanorods by covalent functionalization with positively charged catechol derivatives. *Chemistry* **23**, 17257–17268 (2017).
26. Hwang, C. et al. Enhanced biolubrication on biomedical devices using hyaluronic acid-silica nanohybrid hydrogels. *Colloids Surf. B: Biointerfaces* **184**, 110503 (2019).
27. Bai, Z. et al. Tough and tissue-adhesive polyacrylamide/collagen hydrogel with dopamine-grafted oxidized sodium alginate as crosslinker for cutaneous wound healing. *RSC Adv.* **8**, 42123–42132 (2018).
28. Parashar S. K. S., Murty B. S., Repp S., Weber S. & Erdem E. Investigation of intrinsic defects in core-shell structured ZnO nanocrystals. *J. Appl. Phys.* **111**, 113712 (2012).
29. Rajh, T. et al. Surface restructuring of nanoparticles: an efficient route for ligand−metal oxide crosstalk. *J. Phys. Chem. B* **106**, 10543–10552 (2002).
30. Gan, D. et al. Plant-inspired adhesive and tough hydrogel based on Ag-Lignin nanoparticles-triggered dynamic redox catechol chemistry. *Nat. Commun.* **10**, 1487 (2019).
31. Li, Y. et al. A rose bengal/graphene oxide/PVA hybrid hydrogel with enhanced mechanical properties and light-triggered antibacterial activity for wound treatment. *Materi. Sci. Engi. C* **118**, 111447 (2021).
32. Song, Z., Wu, Y., Wang, H. & Han, H. Synergistic antibacterial effects of curcumin modified silver nanoparticles through ROS-mediated pathways. *Mater. Sci. Eng. C. Mater. Biol. Appl.* **99**, 255–263 (2019).
33. Gao, G., Jiang, Y.-W., Jia, H.-R. & Wu, F.-G. Near-infrared light-controllable on-demand antibiotics release using thermo-sensitive hydrogel-based drug reservoir for combating bacterial infection. *Biomaterials* **188**, 83–95 (2019).
34. Stokes, K. Y. et al. Dietary nitrite prevents hypercholesterolemic microvascular inflammation and reverses endothelial dysfunction. *Am. J. Physiol.-Heart Circulatory Physiol.* **296**, H1281–H1288 (2009).
35. Kim, T. I. et al. Antibacterial activities of graphene oxide-molybdenum disulfide nanocomposite films. *ACS Appl. Mater. Interfaces* **9**, 7908–7917 (2017).
36. Dillen, C. A. et al. Clonally expanded γδ T cells protect against *Staphylococcus aureus* skin reinfection. *J. Clin. Invest.* **128**, 1026–1042 (2018).
37. Berube, B. J. et al. Impact of type III secretion effectors and of phenoxyacetamide inhibitors of type III secretion on abscess formation in a mouse model of pseudomonas aeruginosa infection. *Antimicrob. Agents Chemother.* **61**, e01202-17 (2017).
38. Chen, Y. W. et al. Differentiated epithelial- and mesenchymal-like phenotypes in subcutaneous mouse xenografts using diffusion weighted-magnetic resonance imaging. *Int. J. Mol. Sci.* **14**, 21943–21959 (2013).